



Preparation of metal-organic framework-derived porous carbon and study of its supercapacitive performance

Jianqiang Zhang, Jiechen Xue, Ping Li, Siyun Huang, Huixia Feng, Heming Luo*

School of Petrochemical Engineering, Lanzhou University of Technology, Lanzhou 730050, China

ARTICLE INFO

Article history:

Received 28 December 2017

Received in revised form

9 July 2018

Accepted 15 July 2018

Available online 20 July 2018

Keywords:

Metal-organic frameworks

Activation

Porous carbon

Specific capacitance

ABSTRACT

Metal-organic frameworks are formed via the connection of transition metals with oxygen- or nitrogen-containing organic ligands; the organic ligands are rich in carbon and contain heteroatoms such as N and P. Herein, NMFC-T porous carbon was prepared with $(\text{Ni}_3(\text{BTC})_2(\text{Me}_2\text{NH})_3)$ as the carbon precursor using the strategy of pre-carbonization and KOH activation. Influence of carbonization temperature on properties of NMFC-T porous carbon was investigated, and the electrochemical performance of NMFC-800 porous carbon was studied using a three-electrode system. Results revealed that NMFC-800 porous carbon has a high specific surface area of $1143 \text{ m}^2 \text{ g}^{-1}$ with a mesopore proportion over 80%. Using KOH solution as an electrolyte, the specific capacitance was as high as 211 F g^{-1} at a current density of 1 A g^{-1} , and the capacitance retention was 81.04% after 5000 cycles. NMFC-800 porous carbon has excellent supercapacitive performance and good cycle stability.

© 2018 Elsevier Ltd. All rights reserved.

1. Introduction

Supercapacitors, also known as electric double-layer capacitors or pseudocapacitors, are novel energy storage devices that have attracted much attention because of their short charge and discharge time, good cycle performance, large power density, and environmental friendliness [1–5]. The energy storage principle of a supercapacitor can be divided into two types: (1) the potential difference between the electrodes caused by positive and negative ion adsorptions at the interface of the electrode and solution, and (2) oxidation-reduction reactions of electroactive ions that occur on the electrode surface [6,7].

Currently, preparation of supercapacitor electrodes using porous carbon that has high surface area is one of the most important applications of porous carbon in the field of new energy [8,9]. High specific surface area and well-developed pore structure play crucial roles in rapid charge transfer to form an electric double-layer structure. The pore structure of porous carbon depends mainly on the properties (crystal form, density, surface state, and chemical composition) of the carbon precursor and on the specific activation processes (activator, reaction type, and activation mechanism). Generally, there are two ways to porous carbon,

namely, physical and chemical activation. Of these, chemical activation involves embedding chemical reagents in the internal structure of carbon particles followed by a series of cross-linking polycondensation reactions to form micro-mesopores [10–13].

Metal-organic frameworks are network framework structures formed via the connections of transition metals with oxygen- or nitrogen-containing organic ligands [14–17]. Most organic ligands are rich in carbon and contain heteroatoms such as N and P. Oxides of transition metal ions have pseudocapacitive properties. In recent years, there have mainly been two methods employed to prepare porous carbon using MOFs. One method is the direct carbonization of organic ligands using metal-organic frameworks as the carbon source. A.J. Amali, J.K. Sun, Q. Xu prepared porous carbon as a supercapacitor electrode material via the direct carbonization of ultrasonically synthesized ZIF-8 at 800°C [18]. Results from electrochemical tests indicated that porous carbon prepared using ZIF-8 as the carbon precursor had excellent rate performance (specific capacitance of 251 F g^{-1} at 0.25 A g^{-1}) and cycle stability. The second method introduces organic matter (as the carbon source) into the pores using the porous structure of metal-organic frameworks. P. Zhang, F. Sun, Z. Shen, D. Cao prepared a series of porous carbon using pyrolysis at 950°C with ZIF-7 as the template and with glucose, ethylene glycol, glycerol, and furfuryl alcohol as the carbon sources [19]. The porous carbon prepared from different carbon sources exhibited substantially different morphological patterns and different capacitance performances. In recent years, research

* Corresponding author.

E-mail address: luohm666@163.com (H. Luo).

on metal-organic frameworks has become a hot topic in the fields of hydrogen storage, gas adsorption and separation, sensors, and catalysis [20–26]. However, there are relatively few reports regarding the preparation and supercapacitive properties of porous carbon synthesized using metal-organic frameworks as a carbon precursor. Therefore, this study has important research prospects.

In this work, $\text{Ni}_3(\text{BTC})_2(\text{Me}_2\text{NH})_3$ was synthesized via a hydrothermal method and used as a carbon precursor. Porous carbon with hierarchical structure was then obtained from pre-carbonization of the precursor at a certain temperature and then mixing of the pre-carbonization product and KOH in a certain ratio. Cyclic potential and galvanostatic charge-discharge methods with a three-electrode system were used to characterize the micromorphology and structure and the electrochemical capacitive performance.

2. Experimental

2.1. Preparation of carbon precursor and porous carbon

2.1.1. Synthesis of $\text{Ni}_3(\text{BTC})_2(\text{Me}_2\text{NH})_3$

$\text{Ni}(\text{NO}_3)_2 \cdot 6\text{H}_2\text{O}$ (1.25 g) and $\text{C}_9\text{H}_6\text{O}_6$ (0.60 g) were first placed in a beaker, and then 24.0 mL of DMF was added. After dissolving using magnetic stirring for 5 min at room temperature, 0.90 g of $\text{C}_6\text{H}_5\text{NO}_2$ was added, and the mixture was stirred further for 15 min. The resulting mixture was poured into a 100 mL autoclave reactor and placed in an oven. The reactor was heated in the oven to 150 °C at a rate of 10 °C/h, and then the temperature was maintained for 72 h. Dark green crystals of $\text{Ni}_3(\text{BTC})_2(\text{Me}_2\text{NH})_3$ were obtained after the temperature was cooled to room temperature at a rate of 10 °C/h.

2.1.2. Preparation of porous carbon

An appropriate amount of $\text{Ni}_3(\text{BTC})_2(\text{Me}_2\text{NH})_3$ crystals were placed in a tubular furnace for carbonization under an Ar atmosphere (99.999%) at 600 °C for 2 h (heating rate of 3 °C min⁻¹). Samples of the mixture of pre-carbonized product and KOH (in a ratio of 1:3) was put into a tubular furnace and heated to 700, 750, 800, 850, and 900 °C under an Ar atmosphere (99.999%) with a heating rate of 3 °C min⁻¹. The reactions were kept for 2 h at the according temperatures, and the resulting products were washed with 1 mol L⁻¹ hydrochloric acid and then rinsed with deionized water until the pH was neutral. Porous carbon powder was obtained after drying in vacuum at 80 °C for 12 h. The porous carbon was denoted as NMFC-T, where NMF represents $\text{Ni}_3(\text{BTC})_2(\text{Me}_2\text{NH})_3$ crystals, C represents porous carbon, and T represents the carbonization temperature.

2.2. Characterizations of structure and performance

The morphologies of NMFC-T porous carbon were characterized using scanning electron microscopy (SEM: JSM-5600LV, JEOL) and transmission electron microscopy (TEM: JEM-1200EX, JEOL). The crystal structures were investigated using X-ray diffraction (XRD: RINT-2000, Rigaku Corporation, Japan). The pore structures of NMFC-T porous carbon were characterized using N_2 adsorption/desorption tests (Tristar II 3020, Microtherm Instruments, USA). The specific surface areas (S_{BET}) were calculated using the BET equation on the basis of the adsorption data in the relative pressure (P/P_0) range of 0.06–0.20. The total pore volumes (V_{total}) were determined using the amount of N_2 adsorption at a relative pressure (P/P_0) of 0.97.

2.3. Electrochemical performance measurements

To prepare the working electrode, NMFC-T porous carbon, acetylene black, and polytetrafluoroethylene were uniformly mixed in a mass ratio of 8.5:1:0.5 (about 4 mg) and a slurry was obtained by adding anhydrous ethanol as solvent. The slurry mixture was uniformly coated on nickel foam (1 cm × 1 cm), dried in vacuum at 80 °C for 24 h, and then pressed under a pressure of 15 MPa for about 1.5 min. A three-electrode system was used to measure the electrochemical behaviors, and electrochemical measurements were taken, including cyclic potential, galvanostatic charge/discharge, and electrochemical impedance spectroscopy. The working electrode was a porous carbon electrode, the counter electrode was Pt foil (1.5 cm²), and the reference electrode was the saturated calomel electrode. The electrolyte used in all of the measurements was a 6 mol L⁻¹ KOH solution.

The specific capacitance C (F g⁻¹) was calculated using the galvanostatic charge-discharge curve according to formula (1)

$$C = \frac{I \cdot \Delta t}{m \cdot \Delta V} \quad (1)$$

where I is the charge and discharge current (A), ΔV is the voltage change during discharge (V), Δt is the discharge time (s), and m is the mass of porous carbon on the working electrode (g).

The specific capacitance C (F g⁻¹) was calculated using the cyclic potential curve according to formula (2)

$$C = \frac{\int i(V) dV}{2 \cdot v \cdot m \Delta V} \quad (2)$$

where $i(V)$ is current as a function of voltage and v is the scan rate (mV s⁻¹).

AC impedance was tested in a frequency range from 10 mHz to 100 KHz with an amplitude of 5 mV.

3. Results and discussion

Fig. 1 shows the X-ray diffraction (XRD) patterns of NMFC-T porous carbon. Only two typical diffraction peaks (located at about 25.8° and 43.6°) were observed in the 2θ range of 10°–80° in the XRD patterns. These peaks can be assigned to the (002) and (101) diffraction peaks, respectively, of graphite, and these are consistent with JCPDS 01-0640 card [27]. The presence of the

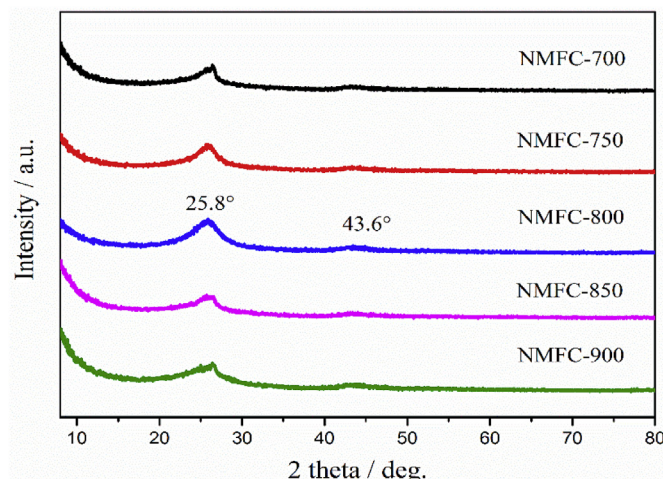


Fig. 1. XRD patterns of NMFC-T porous carbon.

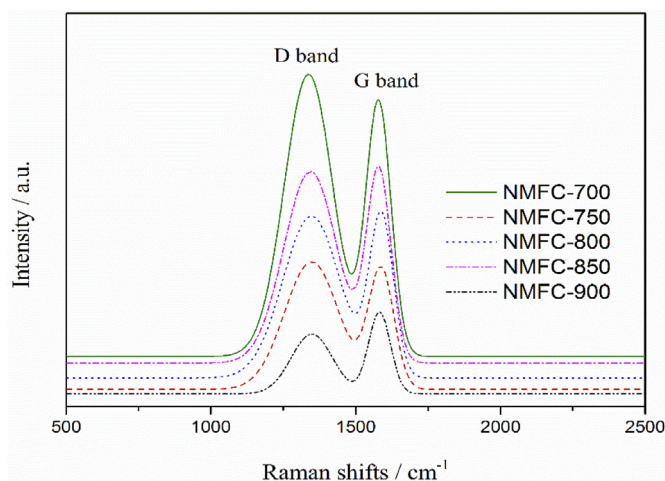


Fig. 2. Raman spectra of NMFC-T porous carbons.

graphite stacking peak at 25.8° indicates that NMFC-T porous carbon has amorphous structure and a low degree of graphitization. A higher degree of interlayer condensation can enhance the conductivity of the material. The diffraction peak at $\sim 25.8^\circ$ (002) of NMFC-T porous carbon is relatively weaker than commercial activated carbon. This is because the graphite crystal structure was destroyed after NMFC-T porous carbon was activated at high temperature by KOH, and thus, a large number of holes appeared on the surface and in the interior. The presence of a weak peak at 43.6° and the low intensity diffraction peak (101) indicated that NMFC-T porous carbon had a carbon nanosheet structure.

Raman spectra reveal the changes in relative intensity, location, width, and shape of the sample peaks. Fig. 2 shows typical Raman spectra of NMFC-T porous carbon, and in each, the D band (1350.1 cm^{-1}) and G band (1586.2 cm^{-1}) are present. The D band is related to the double resonance process of the disordered carbon, and the peak intensity characterizes the number of nongraphitic boundaries in the porous carbon; this indicates that the disordered layer has a nongraphitic structure. The G band is caused by the E_{2g}

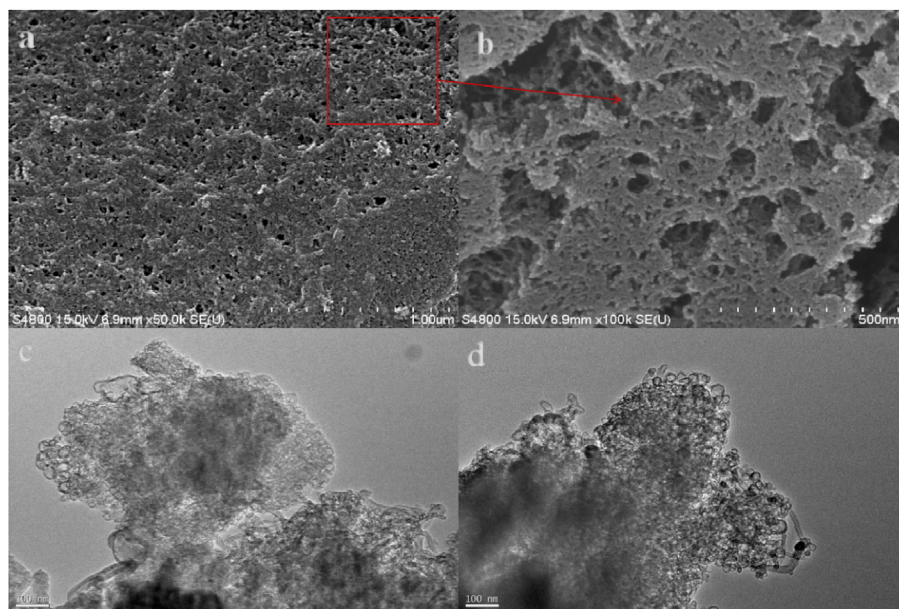


Fig. 3. SEM images (a, b) and TEM images (c, d) of NMFC-800 porous carbon.

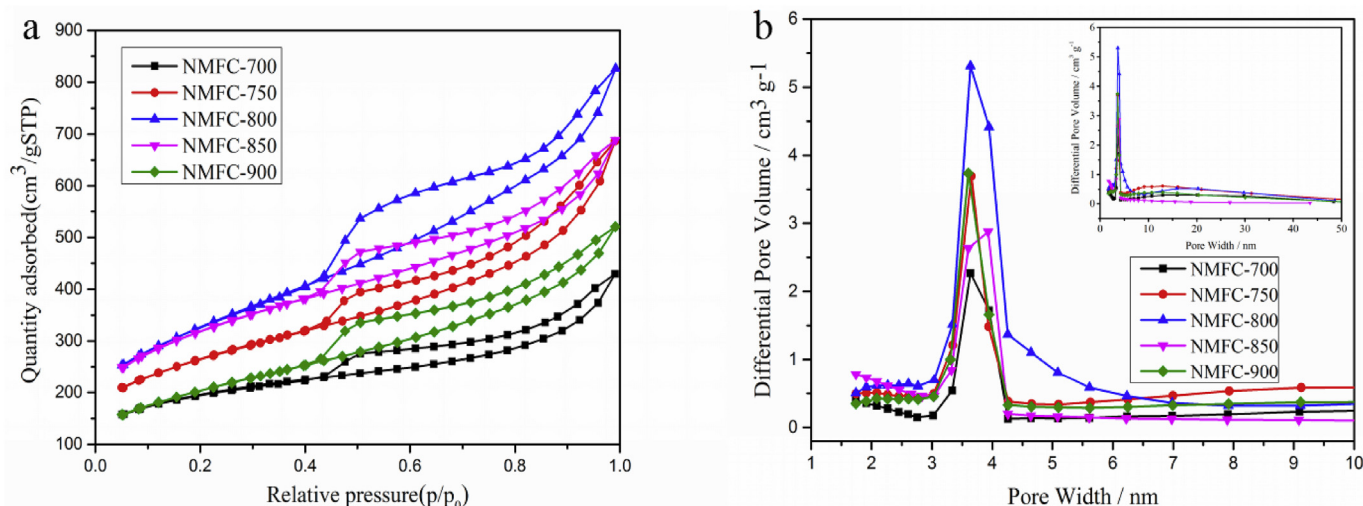


Fig. 4. (a) N_2 adsorption-desorption isotherms and (b) pore size distributions of NMFC-T porous carbons.

Table 1
Values of specific surface area and pore characteristics of YNMFC-600 and NMFC-T.

Sample	S_{BET} ($\text{m}^2 \text{g}^{-1}$)	V_{total} ($\text{cm}^3 \text{g}^{-1}$)	D_{average} (nm)	D_{particle} (nm)
YNMFC-600	203	0.569	21.47	32.97
NMFC-700	656	0.664	4.043	9.134
NMFC-750	911	1.061	4.657	6.581
NMFC-800	1143	1.278	4.472	5.246
NMFC-850	1028	0.742	2.886	5.836
NMFC-900	713	0.805	4.515	8.413

phonon vibration of sp^2 hybrid carbon atoms, and corresponds to complete single crystal graphite [28–31]. Compared to the G band, the peak position, intensity and width of the D band depends on the nature of impurities and functional groups that are associated with the disordered types [32]. The degree of graphitization of porous carbon is calculated as $R = I_D/I_G$ [33–35]. The value of R is proportional to the reciprocal of the size of the graphite microcrystal L_a . When the graphitization degree of porous carbon is higher, the crystallite size and the value of R are smaller. From Fig. 2, it can be observed that the values of the intensity ratio I_D/I_G of the porous carbon (NMFC-700, NMFC-750, NMFC-800, and NMFC-850) were

greater than 1, and this indicates disordered carbon structures. The intensity ratio of NMFC-900 porous carbon was less than 1, and this was because of the gradual increase in the degree of disorder with an increase in temperature.

Fig. 3 displays SEM and TEM images of NMFC-800 porous carbon. SEM images (Fig. 3 (a) and (b)) clearly show that NMFC-800 had a dense porous structure. This was because KOH entered the internal structure of carbon during KOH activation and etched the carbon matrix to form a more porous structure. This resulted in porous carbon that had a higher specific surface area and larger pore volume. From the TEM images (Fig. 3 (c) and (d)), it was found that NMFC-800 porous carbon had a sheet-like nanoporous structure that formed from the stacking of a large number of nanomicroballs. Moreover, micro- and mesopores (with high densities) were distributed in the resulting amorphous sheet-like material, and thus there was a completely disordered porous structure.

As shown in Fig. 4 (a), the adsorption and desorption curves do not coincide, and capillary coalescence occurred with obvious desorption hysteresis in the regions of relatively medium and high pressure. According to IUPAC classification, the adsorption-desorption isotherms of this sample are type IV isotherms [36,37]. The obvious “hysteresis loop” indicates that the pore

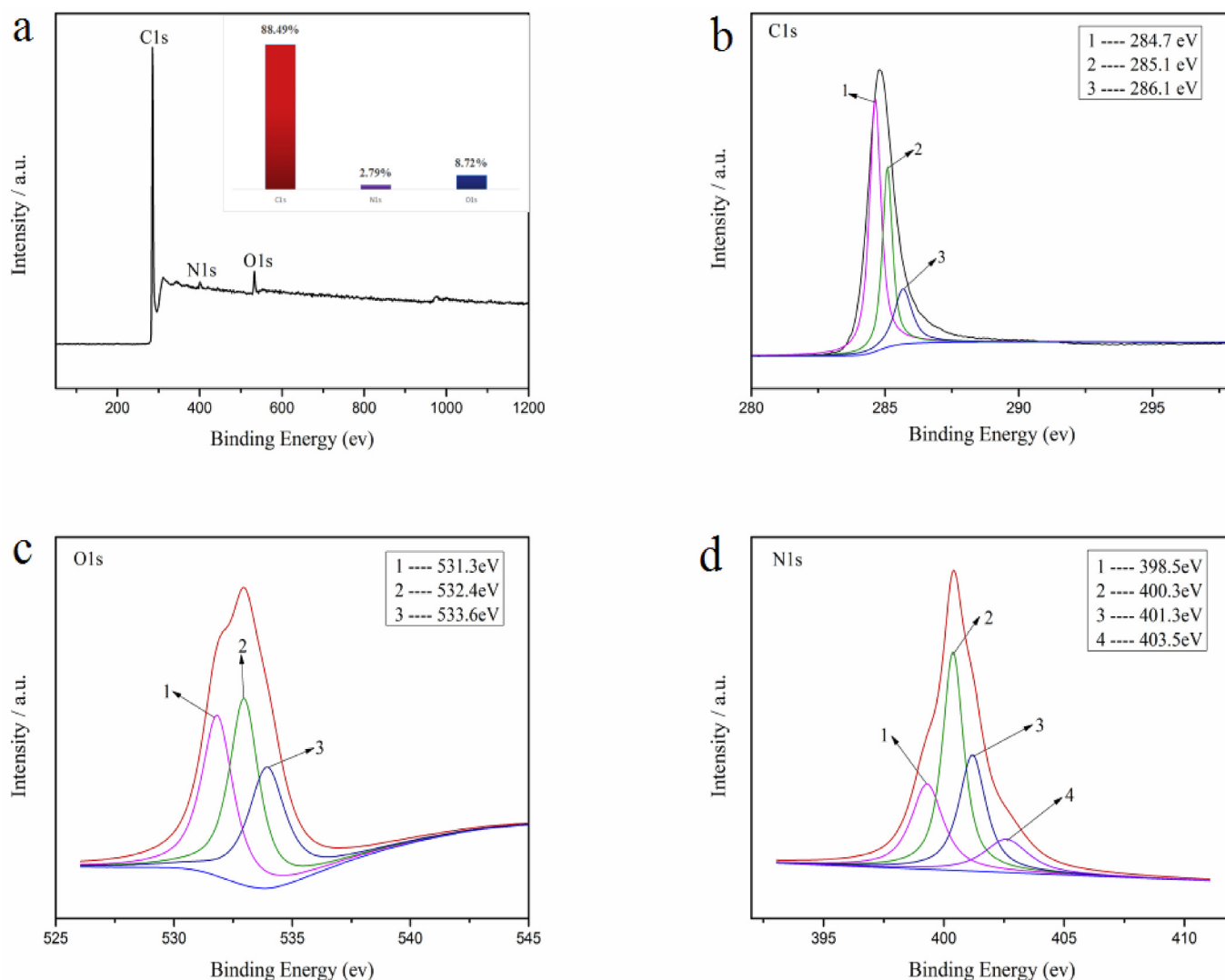


Fig. 5. Well-fitted XPS spectra of NMFC-800 porous carbon: (a) XPS survey spectra and (b) C1s, (c) O1s, and (d) N1s spectra.

structure of NMFC-T porous carbon was mainly composed of mesopores, and this is favorable for storing electrolyte ions in the process of charging and discharging. When the relative pressure was close to 0, the N_2 adsorption capacities tended to increase, and this indicates that there was a certain amount of microporous structure in the NMFC-T porous carbon. When the relative pressure was between 0.45 and 1.0, there were clear hysteresis loops, suggesting that porous carbon has an abundance of mesopores [38]. When the relative pressure was close to 1, the N_2 adsorption/desorption curves were flat, and the adsorption capacity did not increase obviously; this indicates that the proportions of macropores in the porous carbon were small.

As seen in Fig. 4 (b), NMFC-T porous carbon had a relatively small proportion of micropores, and the pore sizes were mostly 1.5–2 nm. The appearance of a large peak at 3–4 nm indicates that the pore sizes of porous carbon were mainly in this range. Only a small amount of pores had volumes larger than 4 nm, and about 80% of these were derived from mesopores. Obviously, NMFC-T porous carbon had a high amount of mesopores. The pore volume characteristics of porous carbon are listed in Table 1. The pore size distribution of YNMFC-600 was the same as that of porous carbon obtained from pre-carbonization. Compared with activated porous carbon, the specific surface area of YNMFC-600 was relatively smaller, and the pore size is larger; this indicates that KOH activation can increase the specific surface area of porous carbon and

can make the pore size distribution more reasonable.

The elemental compositions of NMFC-T porous carbon and the chemical states and electronic states of the elements were investigated using XPS. The XPS spectrum in Fig. 5 (a) shows the chemical characteristics of C1s, N1s, and O1s in NMFC-800 porous carbon. From calculations, the percentages of carbon, nitrogen, and oxygen were determined to be 88.49%, 2.79%, and 8.72%, respectively. Oxygen and nitrogen on the surface of porous carbon can improve the wettability of the electrode material and increase pseudocapacitance, which contributes to an increase in energy density [39]. The C1s spectrum (shown in Fig. 5 (b)) can be fitted into three major peaks. The primary characteristic peak (located at 284.7 eV) corresponds to C=C (284.7 eV). The adjacent peak at 285.1 eV is attributed to C–N and C=N, and the characteristic peak at 286.1 eV corresponds to C–O [40–42]. The O1s spectrum (shown in Fig. 5 (c)) can be divided into three main characteristic peaks. The characteristic peaks at 531.3 eV and 532.4 eV are attributed to the presence of –C=O (ester) and –C=O (carboxyl), respectively, and the characteristic peak at 533.6 eV is ascribed to the presence of O–C=O [43]. The N1s spectrum (shown in Fig. 5 (d)) can be fitted into four major characteristic peaks. The strongest characteristic peak, which is at 400.3 eV, may be caused by the presence of N-5 (pyrrolic-N). Other peaks at 398.5, 401.3, and 403.5 eV correspond to N-6 (pyridinic-N), N-Q (quaternary-N) and N-x (pyridine-N-oxide), respectively [44–46].

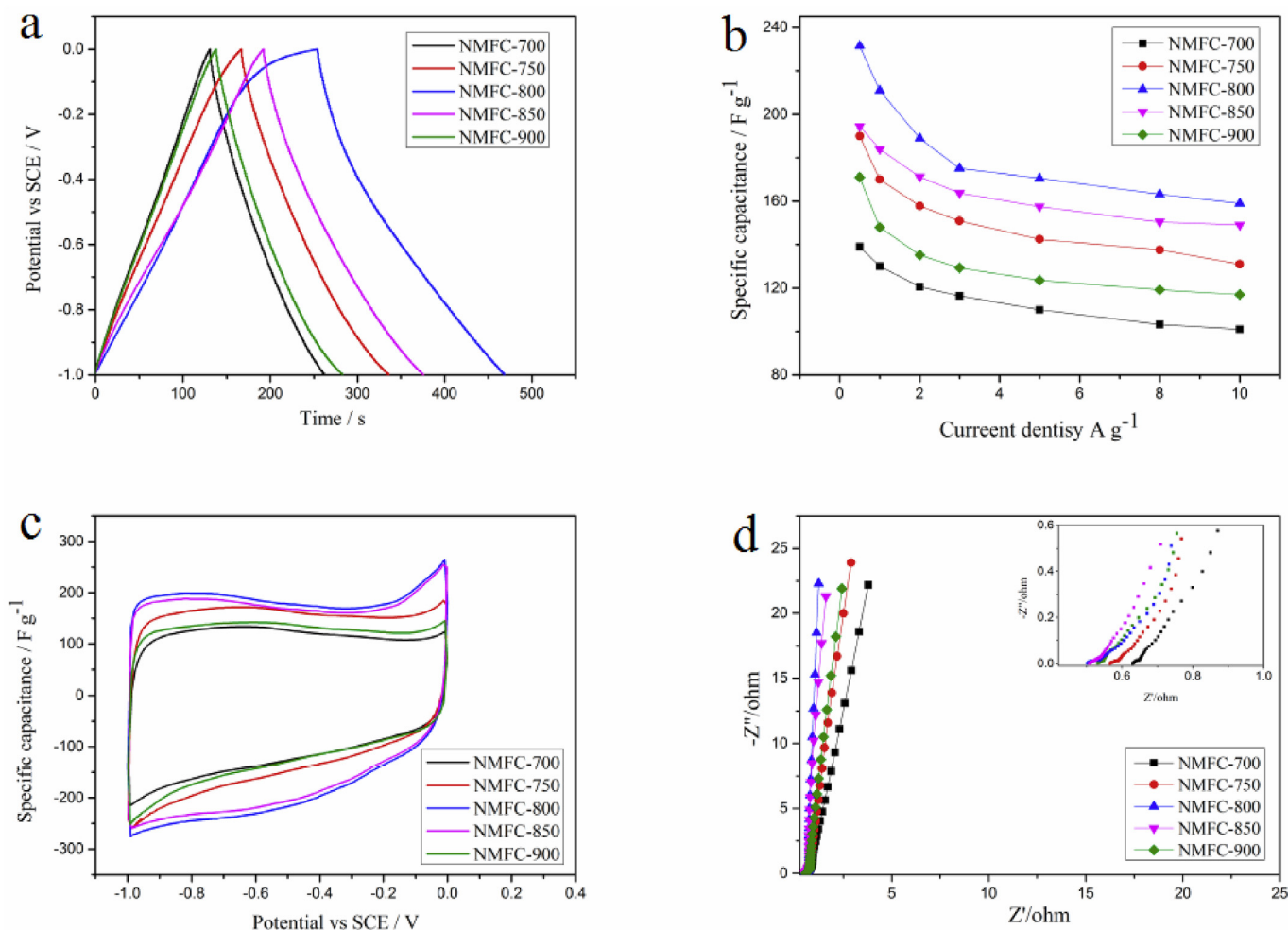


Fig. 6. Results of electrochemical tests for NMFC-T porous carbon: (a) galvanostatic charge/discharge curves of NMFC-T porous carbon at 1.0 A g^{-1} , (b) specific capacitances of NMFC-T porous carbon determined using galvanostatic charge/discharge curve, (c) cyclic potential curves of NMFC-T porous carbon at 10 mV s^{-1} , and (d) Nernst plots.

Fig. 6 (a) shows the galvanostatic charge/discharge curves of NMFC-T porous carbon at a current density of 1.0 A g^{-1} in 6 mol L^{-1} KOH electrolyte prepared using different activation temperatures. As shown in Fig. 6 (a), all of the galvanostatic charge/discharge curves had high symmetry, and this indicates that NMFC-T porous carbon had good capacitive performance. The galvanostatic charge/discharge curve deviated from linearity to some extent, which suggests pseudocapacitive behavior. The specific capacitances calculated using the galvanostatic charge/discharge curves are shown in Fig. 6(b). Obviously, NMFC-800 porous carbon had excellent electrochemical performance and good rate capability. Fig. 6(c) shows the cyclic potential curves of NMFC-T porous carbon in 6 mol L^{-1} KOH electrolyte at a scan rate of 10 mV s^{-1} . There are weak redox peaks in the cyclic potential curves, and these are mainly because of the presence of nitrogen- and oxygen-containing functional groups on the surface of the porous carbon [47]. NMFC-800 porous carbon had the largest integral area for its cyclic potential curve, and this indicates that it had the best specific capacitance. Fig. 6(d) shows the Nernst plots for NMFC-T porous carbon. In the low-frequency region, the curves were almost perpendicular to the real axis, which suggests that the materials had good capacitance behavior. In the high-frequency region, the equivalent series resistances of NMFC-700, NMFC-750, NMFC-800, NMFC-850, and NMFC-900 porous carbon were 0.631 , 0.565 , 0.502 ,

0.508 , and 0.535Ω , respectively. Obviously, NMFC-800 porous carbon had good capacitance behavior in the low-frequency region. This reveals that the hierarchical mesoporous network avoided internal resistance that results from the impediment of ion transport in the electrolyte because of the long and tortuous channels of the micropores.

Fig. 7(a) shows the galvanostatic charge/discharge curves of NMFC-800 porous carbon at different current densities. The good symmetry indicates that the porous carbon had good capacitance and rate capacity. Fig. 7(b) shows the specific capacitances of NMFC-800 porous carbon at different current densities. The specific capacitance was 211 F g^{-1} at a current density of 1 A g^{-1} . When the current density was increased to 10 A g^{-1} , the specific capacitance remained as high as 160 F g^{-1} , and the capacitance retention was as high as 75.8% ; this is consistent with pore size distribution analysis. The presence of specific capacitance was mainly caused by an insufficient diffusion of electrolyte ions at high current densities and adsorption blockage in small pores. Fig. 7 (c) shows the cyclic potential curves of NMFC-800 porous carbon at different scan rates. The cyclic potential curve is relatively rectangular, and it retained this good relatively rectangular feature at 200 mV s^{-1} ; this suggests that NMFC-800 porous carbon had a good supercapacitive performance. Fig. 7(d) shows the results of the cycle stability test of NMFC-800 porous carbon carried out at a current density of 1 A g^{-1} .

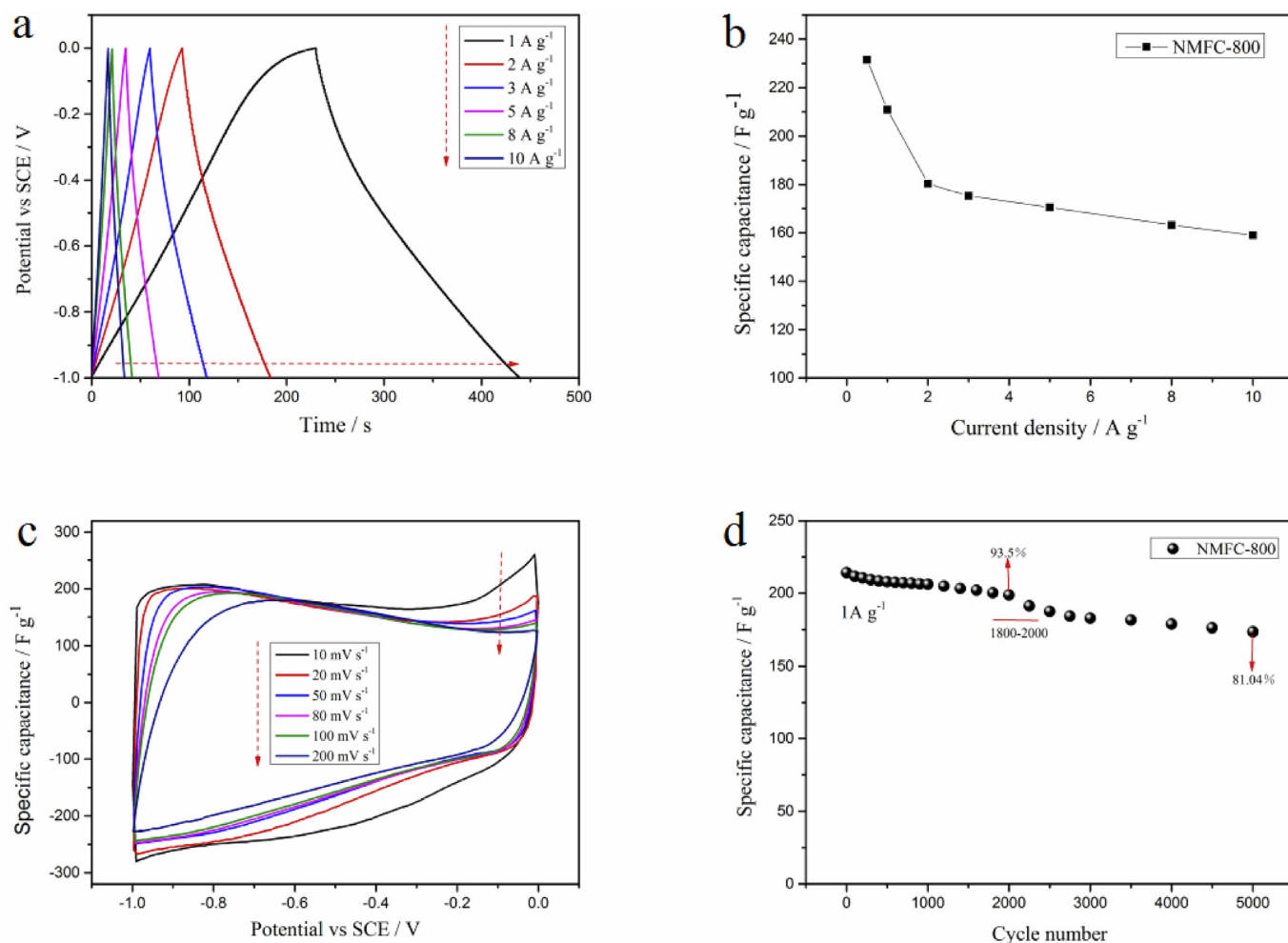


Fig. 7. Electrochemical tests of NMFC-800 porous carbon: (a) galvanostatic charge/discharge curves of NMFC-800 porous carbon at different current densities, (b) specific capacitance of NMFC-800 porous carbon based on galvanostatic charge/discharge curves, (c) cyclic potential curves of NMFC-800 porous carbon at different scan rates, and (d) cycle stability.

The capacitance retention rate was 93.5% for about 2000 cycles. After 2000 cycles, the capacitance retention rate dropped significantly, and this was mainly caused by the poor cycle stability of the nitrogen- and oxygen-containing functional groups in NMFC-800 porous carbon. These functional groups underwent cleavage reactions, and this led to the rapid attenuation of pseudocapacitance. After 5000 charge and discharge cycles, NMFC-800 porous carbon had high electrochemical stability and a relatively high retention of capacitance compared to the capacitance retention rate of 81.04% during the first charge and discharge cycle.

4. Conclusion

In this paper, amorphous structured porous carbon NMFC-T was fabricated via pre-carbonization and KOH activation using a hydrothermally synthesized metal-organic framework compound ($\text{Ni}_3(\text{BTC})_2(\text{Me}_2\text{NH})_3$) as the carbon precursor. Of the prepared samples, NMFC-800 porous carbon had the highest specific surface area ($1143 \text{ m}^2 \text{ g}^{-1}$) and an average pore size of 5.246 nm ; thus, electrolyte ions easily pass through the pores to form electric double-layer capacitance. The specific capacitance of NMFC-800 porous carbon was 211 F g^{-1} at a current density of 1 A g^{-1} , and the capacity retention rate was 81.04% after 5000 charge-discharge cycles. NMFC-800 porous carbon has strong charge storage capacity and good cycle stability, and thus it is expected that it can be used as an excellent electrochemical energy storage material.

Acknowledgements

This work is partially supported by the fund of National Nature Science Foundation of China (No. 21364004 and 21664009) and Gansu Province University Fundamental Research Funds.

References

- [1] Electrochemical Supercapacitors : Scientific Fundamentals and Technological Applications, Plenum Press.
- [2] L. Wang, H. Yang, G. Pan, L. Miao, S. Chen, Y. Song, Polyaniline-carbon nanotubes@zeolite imidazolate framework-67-carbon cloth hierarchical nanostructures for supercapacitor electrode, *Electrochim. Acta* 20 (2017) 16–23.
- [3] E. Frackowiak, F. Béguin, Carbon materials for the electrochemical storage of energy in capacitors, *Carbon* 39 (2001) 937–950.
- [4] M. Sevilla, R. Mokaya, Energy storage applications of activated carbons: supercapacitors and hydrogen storage, *Energy Environ. Sci.* 7 (2014) 1250–1280.
- [5] K. Chen, D. Xue, Ionic supercapacitor electrode materials: a system-level design of electrode and electrolyte for transforming ions into colloids, *Colloids Interface Sci. Commun.* 1 (2014) 39–42.
- [6] B.E. Conway, Transition from 'supercapacitor' to 'battery' behavior in electrochemical energy storage, in: *Power Sources Symposium, 1990.*, Proceedings of the International, 1991, pp. 319–327.
- [7] E. Frackowiak, Carbon materials for supercapacitor application, *Phys. Chem. Chem. Phys.* : *Phys. Chem. Chem. Phys.* 9 (2007) 1774.
- [8] H. Chen, D. Liu, Z. Shen, B. Bao, S. Zhao, L. Wu, Functional biomass carbons with hierarchical porous structure for supercapacitor electrode materials, *Electrochim. Acta* 180 (2015) 241–251.
- [9] L.L. Zhang, X.S. Zhao, Carbon-based materials as supercapacitor electrodes, *Chem. Soc. Rev.* 38 (2009) 2520.
- [10] B. Xu, F. Wu, Y. Su, G. Cao, S. Chen, Z. Zhou, Y. Yang, Competitive effect of KOH activation on the electrochemical performances of carbon nanotubes for EDLC: balance between porosity and conductivity, *Electrochim. Acta* 53 (2008) 7730–7735.
- [11] A. Elmouhahidi, Z. Zapata-Benabithé, F. Carrasco-Marín, C. Moreno-Castilla, Activated carbons from KOH-activation of argan (*Argania spinosa*) seed shells as supercapacitor electrodes, *Bioresour. Technol.* 111 (2012) 185–190.
- [12] H. Teng, Y.-J. Chang, C.-T. Hsieh, Performance of electric double-layer capacitors using carbons prepared from phenol-formaldehyde resins by KOH etching, *Carbon* 39 (2001) 1981–1987.
- [13] J.C.C. Freitas, M.A.S. Jr, A.G. Cunha, F.G. Emmerich, A.C. Bloise, E.R.D. Azevedo, T.J. Bonagamba, NMR investigation on the occurrence of Na species in porous carbons prepared by NaOH activation, *Carbon* 45 (2007) 1097–1104.
- [14] G.K.H. Shimizu, Metal-organic frameworks: model, make, measure, *Nat. Chem.* 2 (2010) 909.
- [15] J.L.C. Rowsell, O.M. Yaghi, Metal-organic frameworks: a new class of porous materials, *Microporous Mesoporous Mater.* 73 (2004) 3–14.
- [16] B. Chen, N.W. Ockwig, A.R. Millward, D.S. Contreras, O.M. Yaghi, High H_2 adsorption in a microporous metal-organic framework with open metal sites, *Angew. Chem.* 44 (2005) 4745–4749.
- [17] M.J. Rosseinsky, Metal-organic frameworks: enlightened pores, *Nat. Mater.* 9 (2010) 609–610.
- [18] A.J. Amali, J.K. Sun, Q. Xu, From assembled metal-organic framework nanoparticles to hierarchically porous carbon for electrochemical energy storage, *Chem. Commun.* 50 (2014) 1519–1522.
- [19] P. Zhang, F. Sun, Z. Shen, D. Cao, ZIF-derived porous carbon: a promising supercapacitor electrode material, *J. Mater. Chem.* 2 (2014) 12873–12880.
- [20] S. Proch, J. Herrmannsdörfer, R. Kempe, C. Kern, A. Jess, L. Seyfarth, J. Senker, Pt@MOF-177: synthesis, room-temperature hydrogen storage and oxidation catalysis, *Chemistry* 14 (2008) 8204.
- [21] R. J.L. S. EC, E. J. H. JA, Y. OM, Gas adsorption sites in a large-pore metal-organic framework, *Science (New York, N.Y.)* 309 (2005) 1350–1354.
- [22] D. Farrusseng, S. Aguado, C. Pinel, Metal-organic frameworks: opportunities for catalysis, *Angew. Chem. Int. Ed.* 48 (2009) 7502–7513.
- [23] J.L.C. Rowsell, A.R. Millward, K.S. P. O.M. Yaghi, Hydrogen sorption in functionalized Metal-Organic frameworks, *J. Am. Chem. Soc.* 126 (2004) 5666–5667.
- [24] W. Chaikittisilp, K. Ariga, Y. Yamauchi, A new family of carbon materials: synthesis of MOF-derived nanoporous carbons and their promising applications, *J. Mater. Chem.* 1 (2013) 14–19.
- [25] K. Xi, S. Cao, X. Peng, C. Ducati, R.V. Kumar, A.K. Cheetham, Carbon with hierarchical pores from carbonized metal-organic frameworks for lithium sulphur batteries, *Chem. Commun.* 49 (2013) 2192–2194.
- [26] L. Xin, Q. Liu, R. Chen, R. Li, Z. Li, J. Wang, Hierarchical metal-organic framework derived nitrogen-doped porous carbon/graphene composite for high performance supercapacitors, *Electrochim. Acta* (2017) 248.
- [27] X. Chen, B. Zhao, Y. Cai, M.O. Tade, Z. Shao, Amorphous V-O-C composite nanofibers electrospun from solution precursors as binder- and conductive additive-free electrodes for supercapacitors with outstanding performance, *Nanoscale* 5 (2013) 12589.
- [28] Y.T. Gong, B.H. Li, T. Pei, C.H. Lin, S. Lee, Raman investigation on carbonization process of metal-organic frameworks, *J. Raman Spectrosc.* 47 (2016) 1271–1275.
- [29] L. Cheng, Y. Hu, D. Qiao, Y. Zhu, H. Wang, Z. Jiao, One-step radiolytic synthesis of heteroatom (N and S) co-doped graphene for supercapacitors, *Electrochim. Acta* 259 (2018) 587–597.
- [30] A. Sadezky, H. Muckenhuber, H. Grothe, R. Niessner, U. Pöschl, Raman microspectroscopy of soot and related carbonaceous materials: spectral analysis and structural information, *Carbon* 43 (2005) 1731–1742.
- [31] A.C. Ferrari, J. Robertson, Interpretation of Raman spectra of disordered and amorphous carbon, *Phys. Rev. B* 61 (2000) 14095–14107.
- [32] Y. Korenblit, M. Rose, E. Kockrick, L. Borchardt, A. Kvit, S. Kaskel, G. Yushin, High-rate electrochemical capacitors based on ordered mesoporous silicon carbide-derived carbon, *ACS Nano* 4 (2010) 1337–1344.
- [33] S.D.M. Brown, P. Corio, A. Marucci, M.A. Pimenta, M.S. Dresselhaus, G. Dresselhaus, Second-order resonant Raman spectra of single-walled carbon nanotubes, *Phys. Rev. B* 61 (2000) 7734–7742.
- [34] G. Gouadec, P. Colombari, Raman Spectroscopy of nanomaterials: how spectra relate to disorder, particle size and mechanical properties, *Prog. Cryst. Growth Char. Mater.* 53 (2007) 1–56.
- [35] J.M. Caridad, F. Rossella, V. Bellani, M.S. Grandi, E. Diez, Automated detection and characterization of graphene and few-layer graphite via Raman spectroscopy, *J. Raman Spectrosc.* 42 (2011) 286–293.
- [36] J. Paz Ferreira, J.G.V. Miranda, E. Vidal Vázquez, Characterizing Nitrogen adsorption and desorption isotherms in soils using multifractal analysis, *Egu Gen. Assemb.* 12 (2010) 2710.
- [37] M. Thommes, K. Kaneko, A.V. Neimark, J.P. Olivier, F. Rodriguezreinoso, J. Rouquerol, K.S.W. Sing, Physisorption of gases, with special reference to the evaluation of surface area and pore size distribution (IUPAC Technical Report), *Chem. Int.* 38 (2011), 25–25.
- [38] F. Li, M. Morris, K.Y. Chan, Electrochemical capacitance and ionic transport in the mesoporous shell of a hierarchical porous core-shell carbon structure, *J. Mater. Chem.* 21 (2011) 8880–8886.
- [39] L. Hao, X. Li, L. Zhi, Carbonaceous electrode materials for supercapacitors, *Adv. Mater.* 25 (2013) 3899–3904.
- [40] S. Kulkarni, U. Patil, I. Shackery, J. Sohn, S. Lee, B. Park, S. Jun, High-performance supercapacitor electrode based on a polyaniline nanofibers/3D graphene framework as an efficient charge transporter, *J. Mater. Chem.* 2 (2014) 4989–4998.
- [41] V. Datsyuk, M. Kalyva, K. Papagelis, J. Parthenios, D. Tasis, A. Siokou, I. Kallitsis, C. Galiotis, Chemical oxidation of multiwalled carbon nanotubes, *Carbon* 46 (2008) 833–840.
- [42] F. Ye, B. Zhao, R. Ran, Z. Shao, Facile mechanochemical synthesis of nano SnO_2 /graphene composite from coarse metallic Sn and graphite oxide: an outstanding anode material for lithium-ion batteries, *Chemistry* 20 (2014) 4055–4063.
- [43] D. Hulicova-Jurcakova, M. Seredych, Q.L. Gao, T.J. Bandosz, Combined effect of nitrogen- and oxygen-containing functional groups of microporous activated carbon on its electrochemical performance in supercapacitors, *Adv. Funct. Mater.* 19 (2009) 438–447.
- [44] R.J.J. Jansen, H.V. Bekkum, XPS of nitrogen-containing functional groups on

- activated carbon, *Carbon* 33 (1995) 1021–1027.
- [45] X. Fan, L. Zhang, G. Zhang, Z. Shu, J. Shi, Chitosan derived nitrogen-doped microporous carbons for high performance CO₂ capture, *Carbon* 61 (2013) 423–430.
- [46] A. Sánchez-Sánchez, F. Suárez-García, A. Martínez-Alonso, J. Tascón, Aromatic polyamides as new precursors of nitrogen and oxygen-doped ordered mesoporous carbons, *Carbon* 70 (2014) 119–129.
- [47] X. Li, J. Wang, Y. Zhao, F. Ge, S. Komarneni, Z. Cai, Wearable solid-state supercapacitors operating at high working voltage with a flexible nanocomposite electrode, *ACS Appl. Mater. Interfaces* 8 (2016) 25905–25914.